Supporting information for

Bimetallic Alloy Ag@Au Nanorings with Hollow Dual-Rims focus Near-Field on Circular Intra-Nanogaps

Sungwoo Lee,[a†] Insub Jung,[a†] Soohyun Lee,[a] Jaewon Lee,[a] Myeong jin Oh,[a] Minsun Park,[a] Jeongwon Kim,[a] MohammadNavid Haddadnezhad,[a] Woocheol Park,[a] and Sungho Park[a,*]

[a]Department of Chemistry, Sungkyunkwan University (SKKU), Suwon, 16419, South Korea

*Email: spark72@skku.edu

†: these authors contributed equally

Table of Contents

Results and Discussion

Supplementary Note 1. Synthetic procedure of Pt dual-rim nanorings (DRNs).

The entire synthetic procedure for the synthesis of Pt DRNs includes of 6 steps: (1) selective etching of Au, (2) edge-selective deposition of Pt, (3) selective etching of Au, (4) eccentric growth of Au, (5) edge-selective deposition of Pt, and (6) selective etching of Au. The detail chemistry of synthetic step is described in our previous literature.[1] We adopted triangular Au nanoplates as starting templates. In step 1 (selective etching of Au), we selectively etched three protruding tips of triangular Au nanoplates with Au^{3+} ions to prepare circular Au nanoplates. In step 2 (edge-selective deposition of Pt), Pt^{4+} ions were preferentially reduced along the periphery of the circular Au nanoplates, which resulted in the synthesis of Au@Pt nanodisks. In step 3 (selective etching of Au), we etched the central Au part of Au@Pt nanodisks with Au^{3+} ions, while leaving a thin Au layer (which is not oxidized with mild Au^{3+} ions etchant) at the inner boundary of Pt single-rim nanorings (SRNs). In step 4 (eccentric growth of Au), Au^{3+} ions were dominantly reduced under the slow kinetic growth condition in an inward fashion starting from the inner boundary of Pt SRNs. Au^{3+} ions are selectively reduced from the Au thin layer at the inner periphery of Pt SRNs, which is attributed to the larger lattice mismatch between Pt and Au (i.e., the lattice constants of Pt and Au are 0.3912 nm, and 0.4065 nm, respectively). In step 5 (edge-selective deposition of Pt), we reduced Pt^{4+} ions at both the outer Pt domain and inner periphery of the Au domain of Pt@Au nanorings to synthesize Pt@Au@Pt nanorings. In step 6 (selective etching of Au), Pt DRNs were synthesized after selective etching of inner Au. The field-emission scanning electron microscopy (FE-SEM) images of triangular Au nanoplates, circular Au nanoplates, Au@Pt nanodisks, Pt SRNs, Pt@Au nanorings, Pt@Au@Pt nanorings, and Pt DRNs are shown in Figure 2A-G.

Supplementary Note 2. Calculation of the enhancement factor of a Ag@Au hollow DRN

We estimated the enhancement factor of a Ag@Au hollow DRN (total diameter = 142 (±7) nm, nanogap size = 11 (±2) nm) using an equation in the previously reported literature: [2, 3]

$$EF = I_{surface} \times N_{solution} / N_{surface} \times I_{solution}.$$

$I_{surface}$ and $N_{surface}$ are the Raman intensity of the Ag@Au hollow DRN and the number of 2-naphthalenethiol molecules adsorbed on the Ag@Au hollow DRN, respectively. $I_{solution}$ and $N_{solution}$ are the normal Raman intensity of 2-naphthalenethiol liquid and the number of 2-naphthalenethiol molecules in the focus of the laser beam, respectively. The SERS peak at 1069 cm^{-1} was chosen for EF calculations.
We estimated $N_{solution}$ using the following equation:

$$N_{solution} = (V \times d \times N_A) / M_w = 2.6 \times 10^{12}.$$

V is effective excitation volume (5.9×10^{-16} m^3), d is the density of 2-naphthalenethiol (1.2 g/cm^3), M_w is the molecular weight of 2-naphthalenethiol (160.23 g/mol), and N_A is Avogadro's number (6.02×10^{23} /mol).

$N_{surface}$ was estimated using the following equation:

$$N_{surface} = A \times D \times N_A = 1.34 \times 10^4$$

A is the active surface area of a Ag@Au hollow DRN (2.03×10^{-14} m^2) and D is the estimated coverage of 2-naphthalenethiol molecules on a Ag@Au hollow DRN (1.1×10^{-10} mol/cm^2).[4]
Based on the equation, the enhancement factor for the Ag@Au hollow DRN is 1.4×10^9.

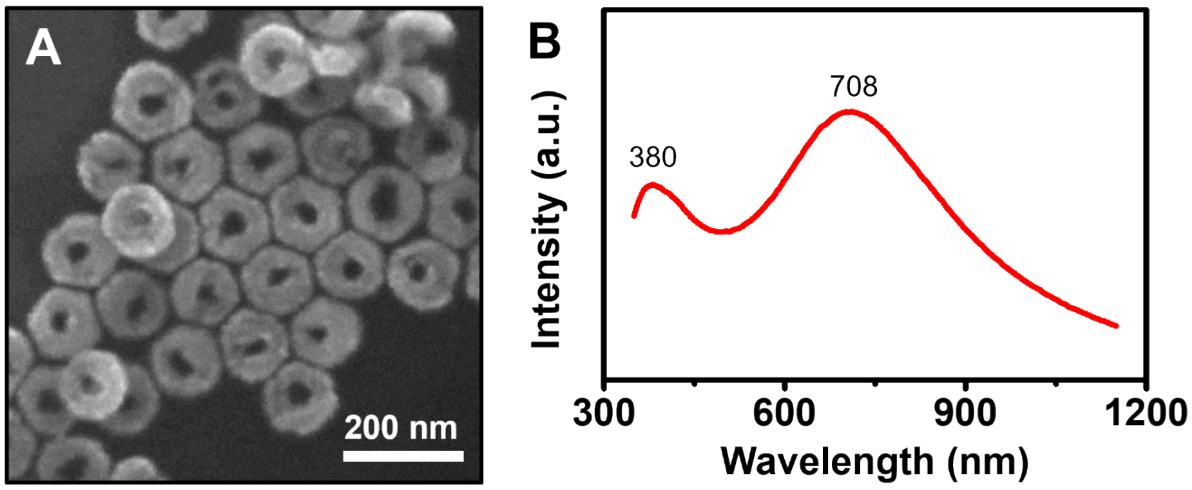

Figure S1. A FE-SEM image and UV-vis-NIR spectrum of Ag SRNs. (A) A FE-SEM image and (B) corresponding UV-vis-NIR spectrum of Ag SRNs. When we reduced Ag^+ on the Pt DRNs under a bromide environment (under the slow kinetic growth condition, $E°[Ag/AgBr] = 0.071$ V), the Ag^+ was reduced in an eccentric fashion, resulting in single Ag SRNs. The UV-vis-NIR spectrum of Ag SRNs showed an in-plane dipole mode at 708 nm and out-of-plane dipole mode at 380 nm.

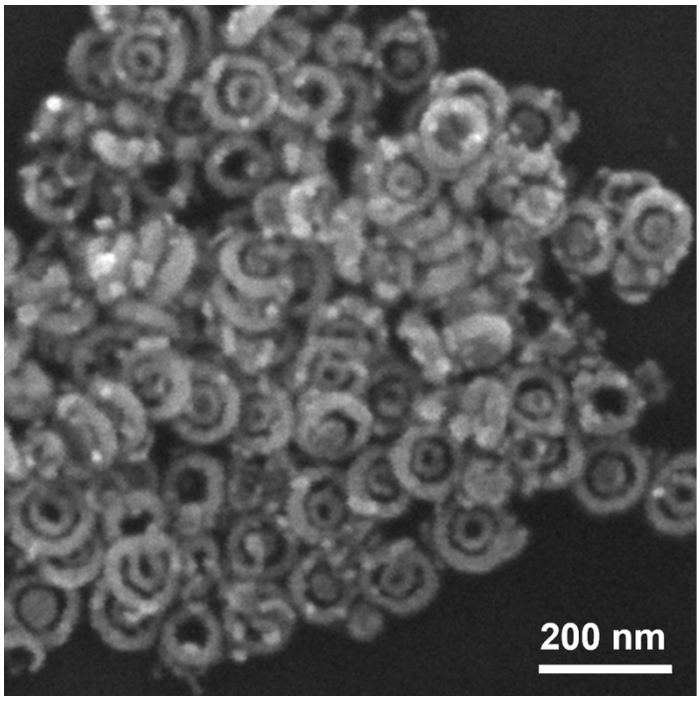

Figure S2. A FE-SEM image of Ag DRNs with Au debris. When we introduced Au^{3+} to the Ag DRN solution without ascorbic acids, we observed spherical Au debris around the Ag DRNs due to the Galvanic replacement reaction between Ag layer of Ag DRNs and Au^{3+}.

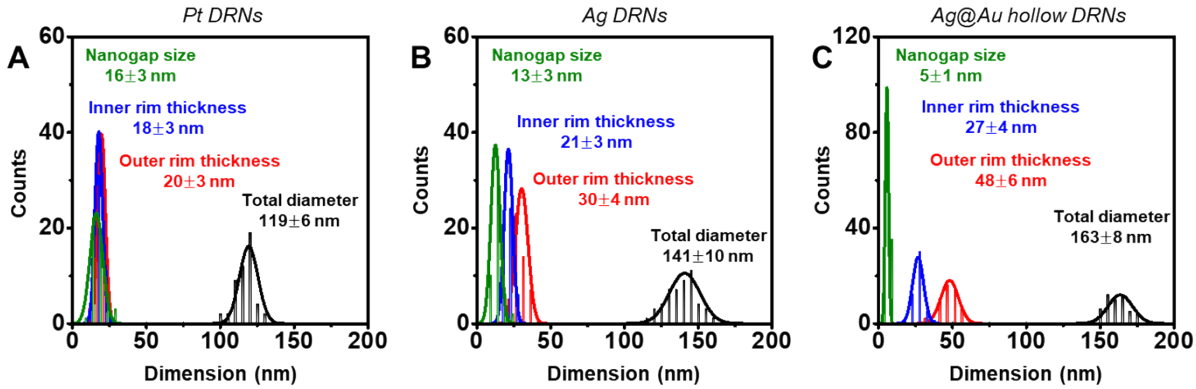

Figure S3. Size distribution histogram of Pt DRNs, Ag DRNs, and Ag@Au hollow DRNs. Size distribution histogram of (A) Pt DRNs, (B) Au DRNs, and (C) Ag@Au hollow DRNs. Starting from Pt DRNs, intra-nanogaps decreased from 16±3 nm, 13±3 and to 5±1 nm after sequential Ag and Au depositions.

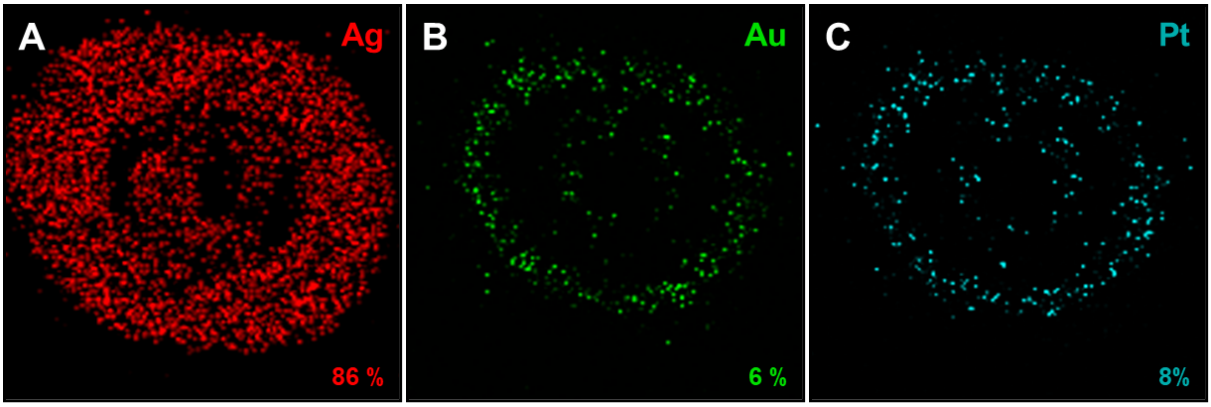

Figure S4. Energy-dispersive spectroscopy (EDS) mapping images of a Ag DRN. EDS mapping images which represent the elemental distributions of (A) Ag, (B) Au and (C) Pt of a Ag DRN.

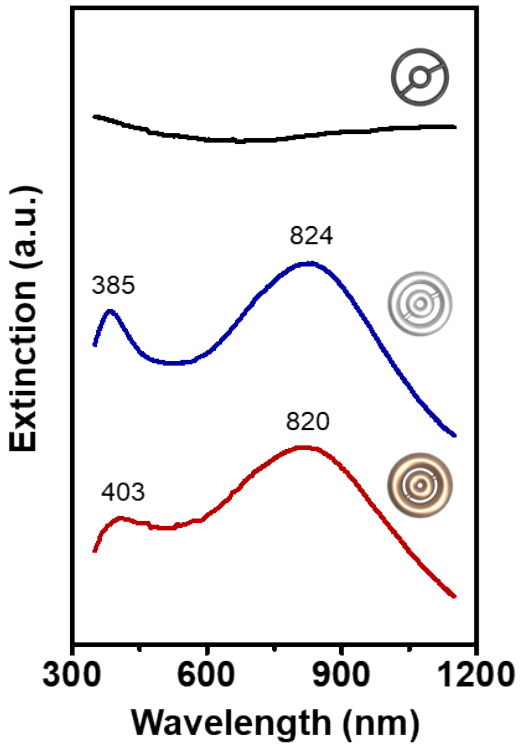

Figure S5. UV-vis-NIR spectra of DRNs. UV-vis-NIR spectra of Pt DRNs (black trace), Ag DRNs (blue trace), and Ag@Au hollow DRNs (red trace).

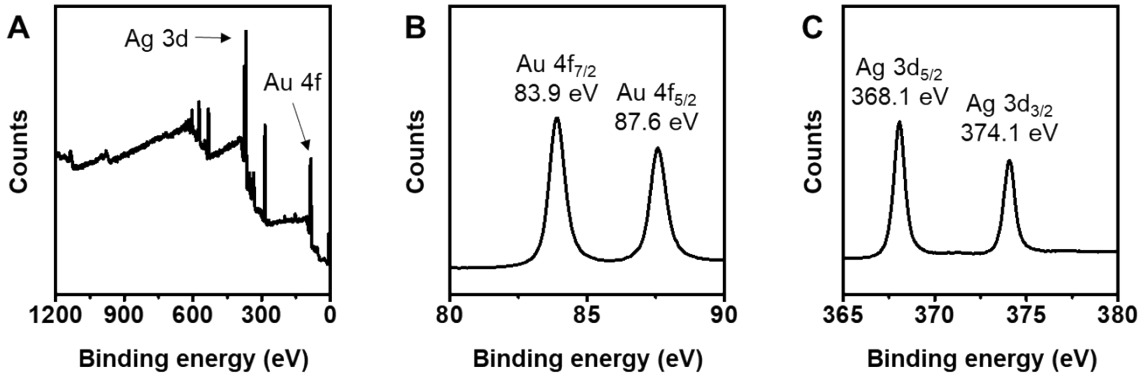

Figure S6. X-ray photoelectron spectroscopy (XPS) data of Ag@Au hollow DRNs (thickness of Ag-Au shell layer: ~2 nm). XPS spectrum of (A) Ag@Au hollow DRNs (thickness of Ag-Au shell layer: ~2 nm) with Ag/Au ratio of 1.94. XPS spectrum of (B) Au 4f and (C) Ag 3d of Ag@Au hollow DRNs.

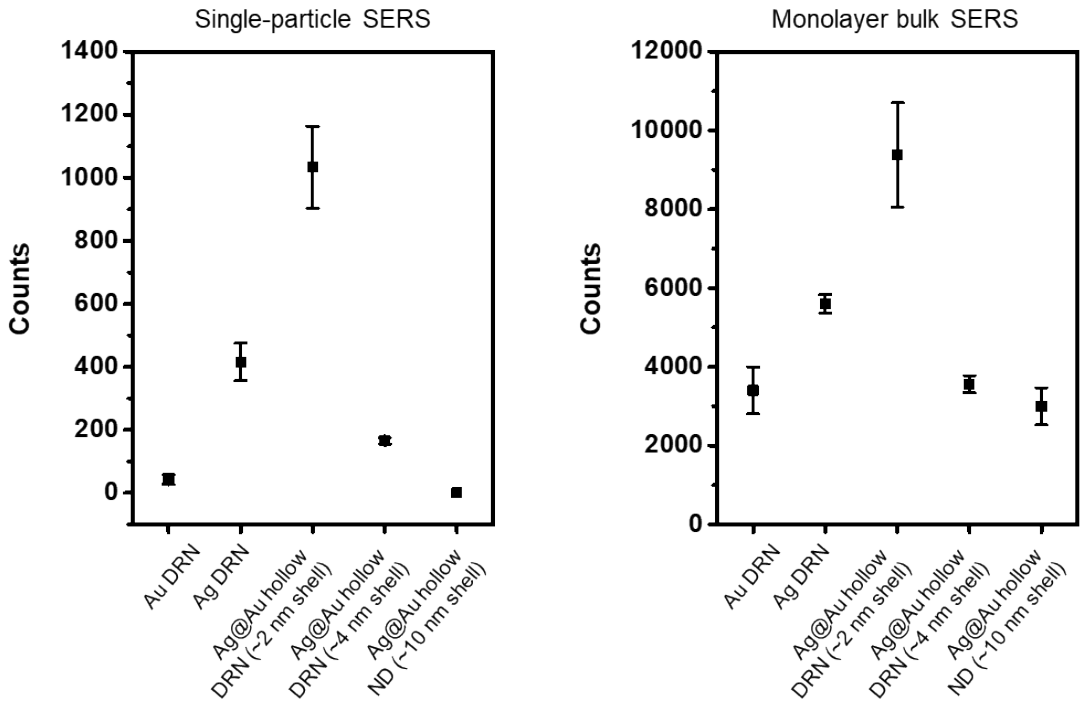

Figure S7. Single-particle SERS and monolayer bulk SERS measurement of Au DRN, Ag DRN, Ag@Au hollow DRN (~2 nm shell), Ag@Au hollow DRN (~4 nm shell), and Ag@Au hollow ND (~10 nm shell). Intensity plot of SERS signals from single-particle SERS and monolayer bulk SERS (The intensity was plotted based on the peak at 1069 cm^{-1}). The error bars represent standard deviation (n=3).

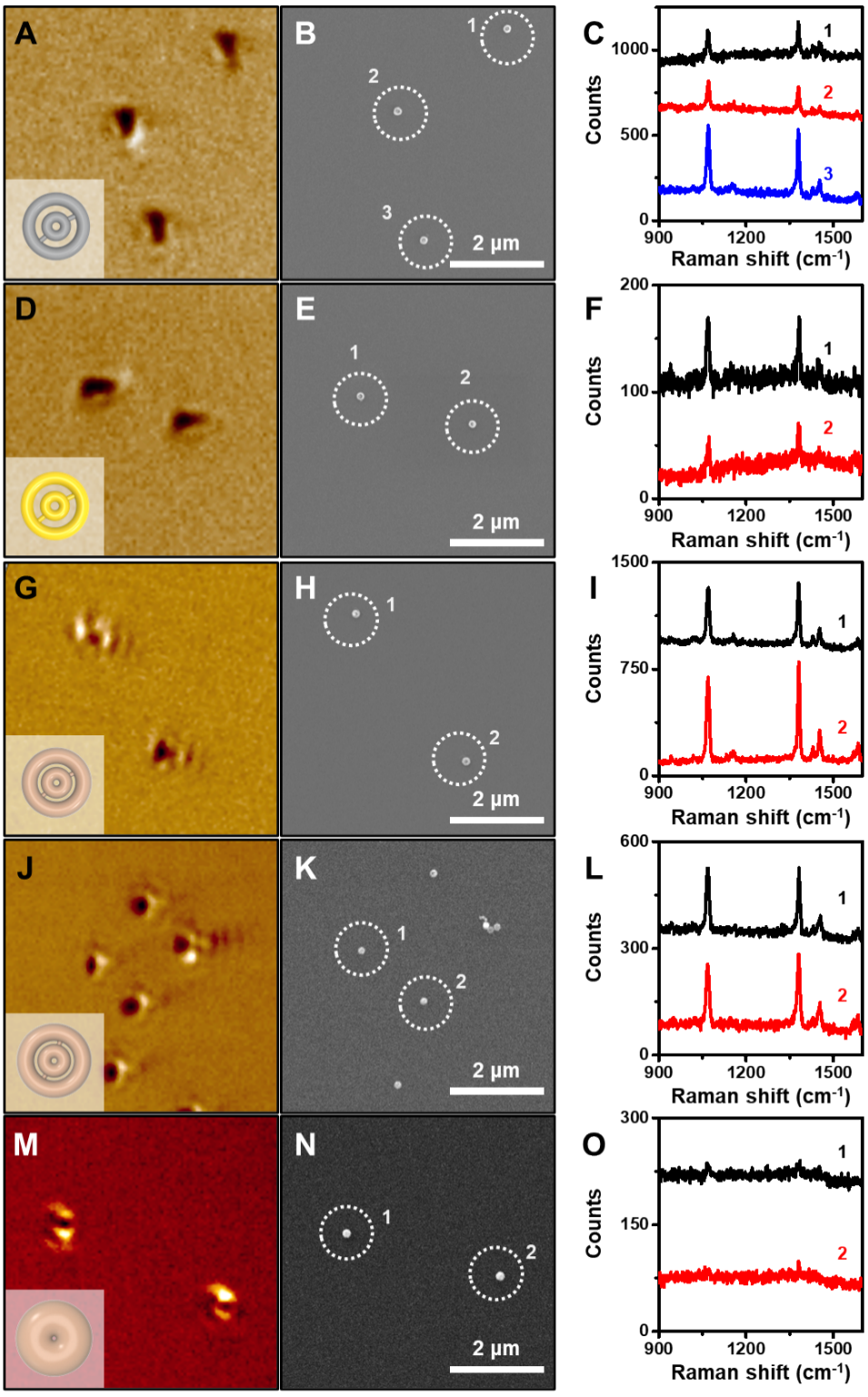

Figure S8. Single-particle SERS spectra of Ag DRNs, Au DRNs, and Ag@Au hollow DRNs. Rayleigh scattering images, corresponding FE-SEM images, and single-particle SERS measurements of 2-NTT from (A-C) Ag DRNs, (D-F) Au DRNs, (G-I) Ag@Au hollow DNRs (thickness of Ag-Au shell layer: ~2 nm), (J-L) Ag@Au hollow DNRs (thickness of Ag-Au shell layer: ~4 nm), and (M-O) Ag@Au hollow nanodisks (thickness of Ag-Au shell layer: ~10 nm).

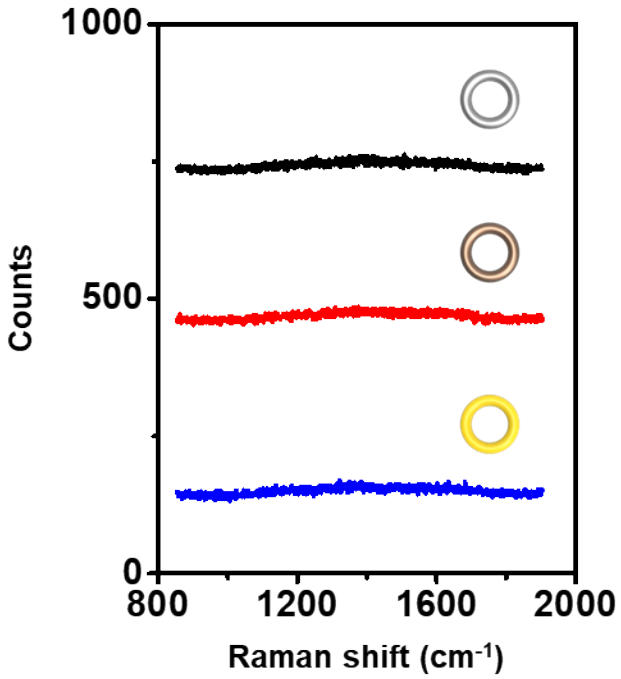

Figure S9. Single-particle SERS spectra of Ag SRNs, Ag@Au hollow SRNs, and Au SRNs. Single-particle SERS measurements of 2-NTT from a Ag SRN (black trace), a Ag@Au hollow SRN (red trace), and a Au SRN (blue trace), respectively.

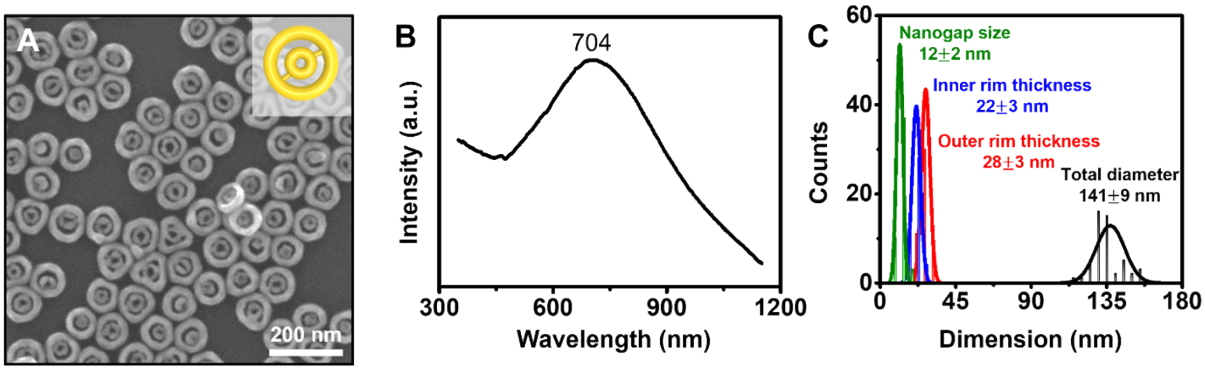

Figure S10. Synthesis of Au DNRs. (A) A FE-SEM image, (B) UV-vis-NIR spectrum, and (C) size distribution histogram of Au DNRs.

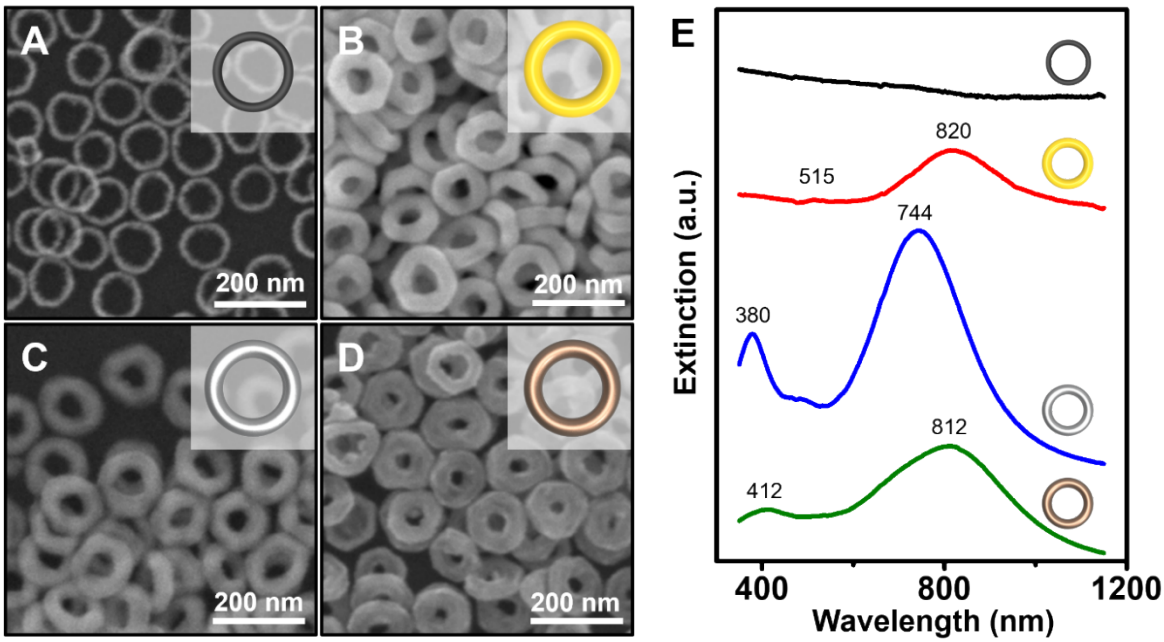

Figure S11. FE-SEM images and UV-vis-NIR spectra of Pt SRNs, Au SRNs, Ag SRNs, and Ag@Au hollow SRNs. FE-SEM images of (A) Pt SRNs, (B) Au SRNs, (C) Ag SRNs, and (D) Ag@Au hollow SRNs and (E) their corresponding UV-vis-NIR spectra.

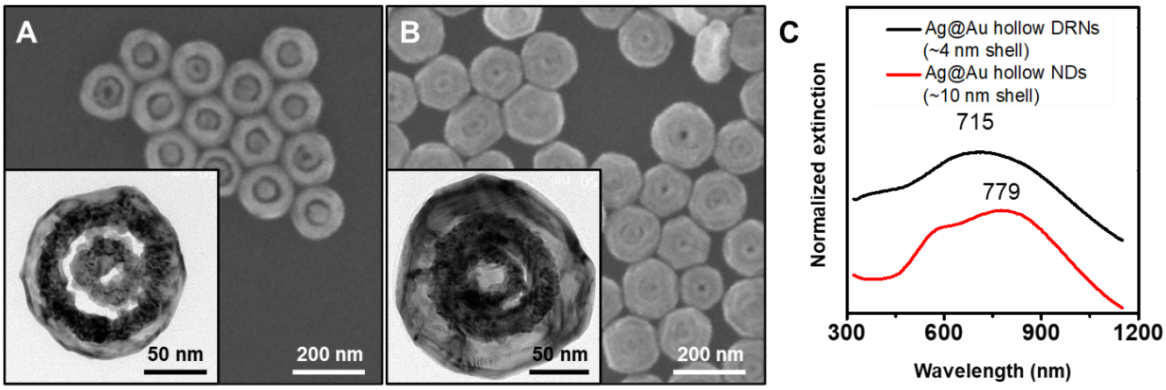

Figure S12. Synthesis and characterization of Ag@Au hollow DRNs with varying Ag-Au shell layer thickness. FE-SEM images and TEM images of (A) Ag@Au hollow DRNs (the thickness of Ag-Au shell layer: ~4 nm) and (B) Ag@Au hollow nanodisks (NDs, the thickness of Ag-Au shell layer: ~10 nm) and (C) corresponding UV-vis-NIR spectrum of nanoparticles. The sizes of nanogaps were estimated using image J program.

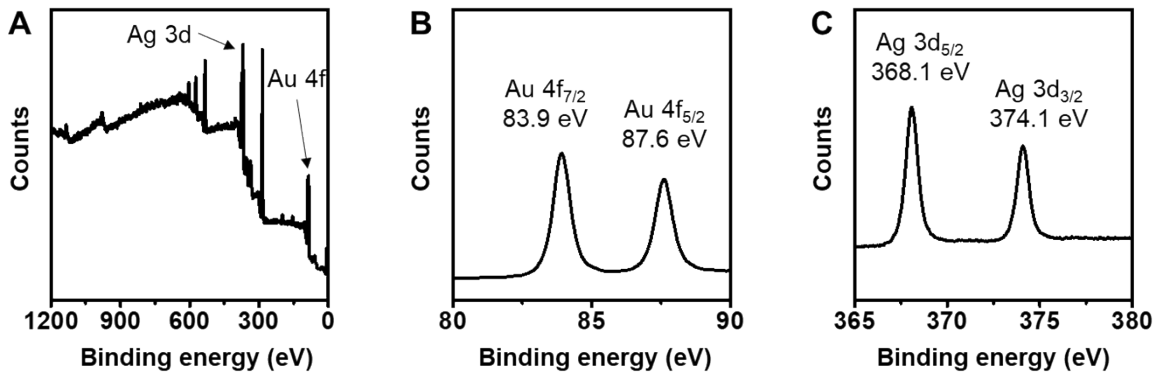

Figure S13. X-ray photoelectron spectroscopy (XPS) data of Ag@Au hollow DRNs (thickness of Ag-Au shell layer: ~4 nm). XPS spectrum of (A) Ag@Au hollow DRNs (thickness of Ag-Au shell layer: ~4 nm) with Ag/Au ratio of 1.65. XPS spectrum of (B) Au 4f and (C) Ag 3d of Ag@Au hollow DRNs.

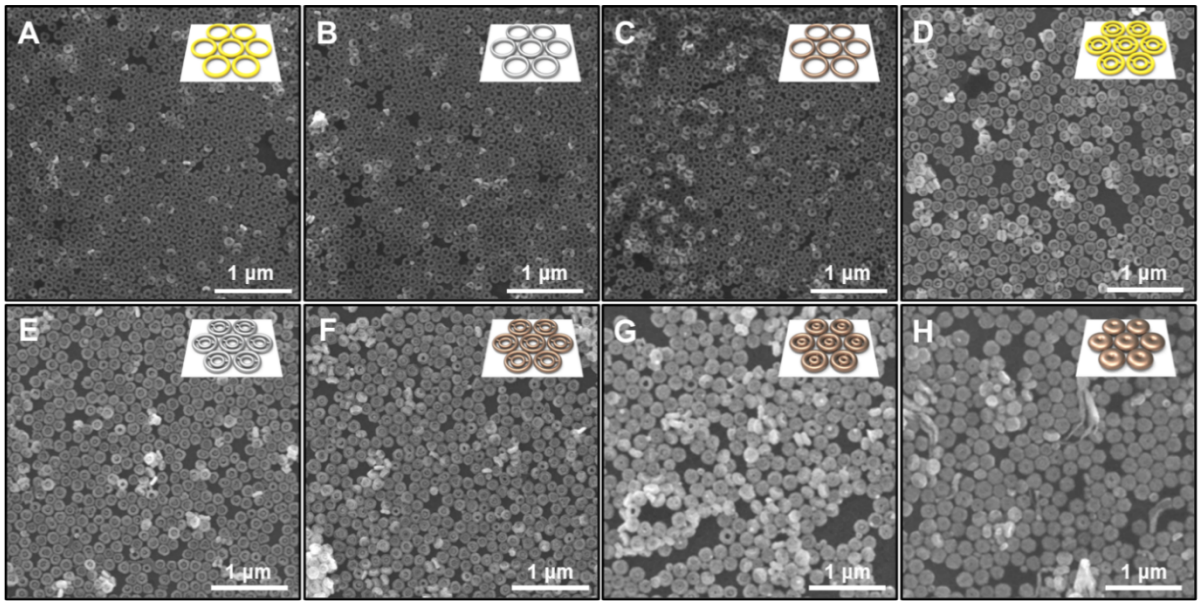

Figure S14. 2D monolayers of SRNs and DRNs formed by the Langmuir-Blodgett method. FE-SEM images of 2D monolayer of (A) Au SRNs, (B) Ag SRNs, (C) Ag@Au hollow SRNs, (D) Au DRNs, (E) Ag DRNs, (F) Ag@Au hollow DRNs (~2 nm shell), (G) Ag@Au hollow DRNs (~4 nm shell), and (H) Ag@Au hollow NDs (~10 nm shell).

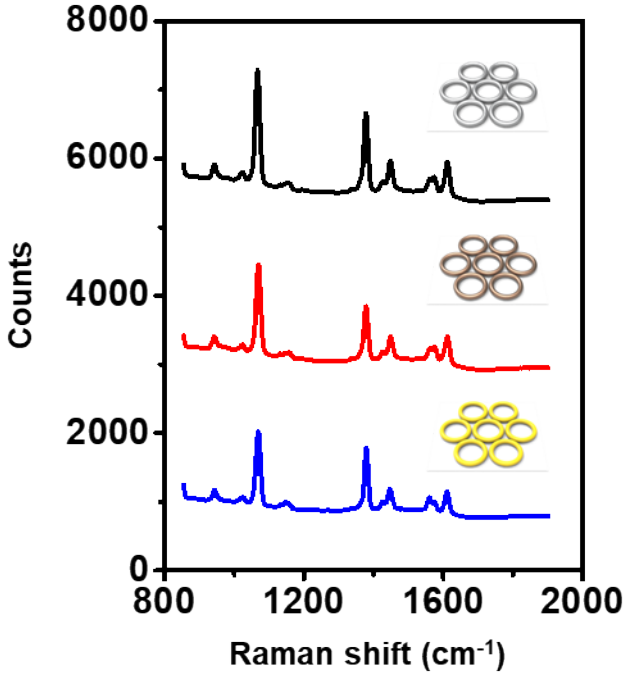

Figure S15. Bulk SERS measurement from 2D monolayer of Ag SRNs, Ag@Au hollow SRNs, and Au SRNs. We performed SERS measurement with 2D monolayer of Ag SRNs (black trace), Ag@Au hollow SRNs (red trace), and Au SRNs (blue trace) on the Si wafer (laser power: 4 mW, analyte: 2-naphthalenethiol).

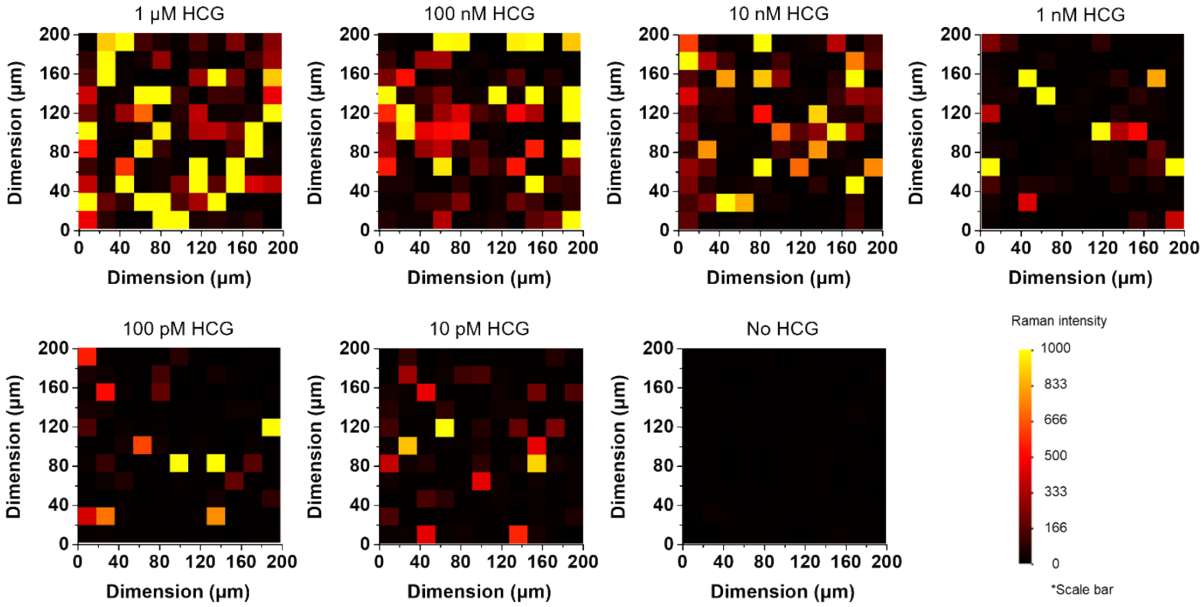

Figure S16. SERS mapping images obtained from SERS-based immunoassay using Ag@Au hollow DRNs. SERS mapping images obtained from SERS-based immunoassay (size: 200 μm × 200 μm, interval: 20 μm) with Ag@Au hollow DRNs for detection of varying concentration of HCG hormones. As the concentration of HCG hormones decreased from 1 μM to 10 pM, SERS peak intensity and the number of SERS-active areas from SERS mapping data consequently decreased. The number of Raman active Ag@Au hollow DRNs on the Au coated silicon wafers increased due to the increased probability of immunochemical reaction between antigens bound at the Au-coated silicon wafers and the antibodies decorated at the Ag@Au hollow DRNs.

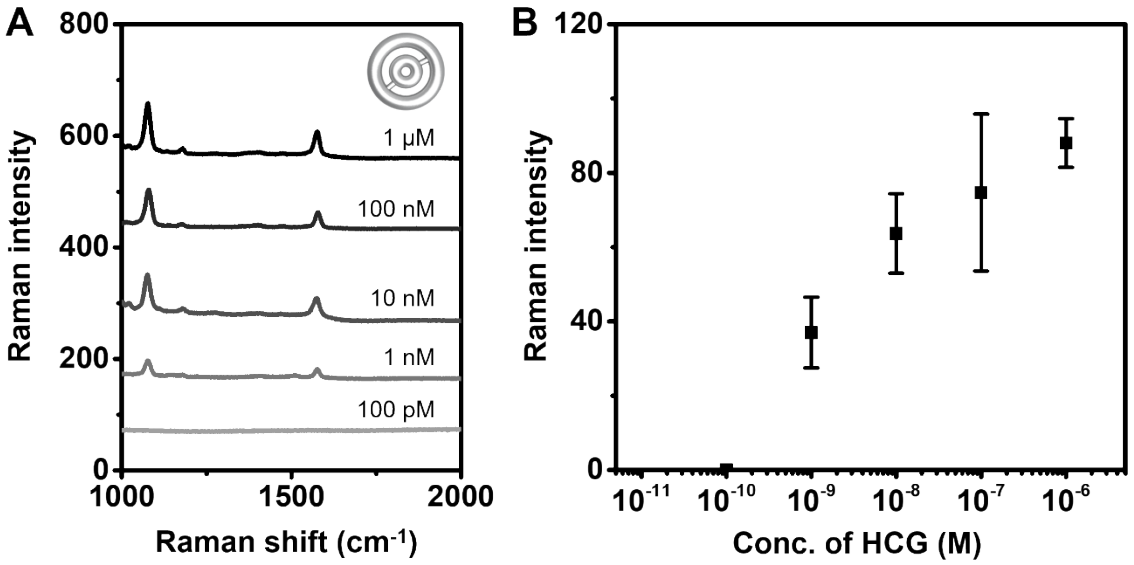

Figure S17. SERS-based immunoassay using Ag DRNs. (A) SERS-spectra obtained from SERS-based immunoassay using Ag DRNs at the varying concentration of HCG hormones and (B) corresponding LOD plot (The intensity was plotted based on the peak at 1080 cm^{-1}).

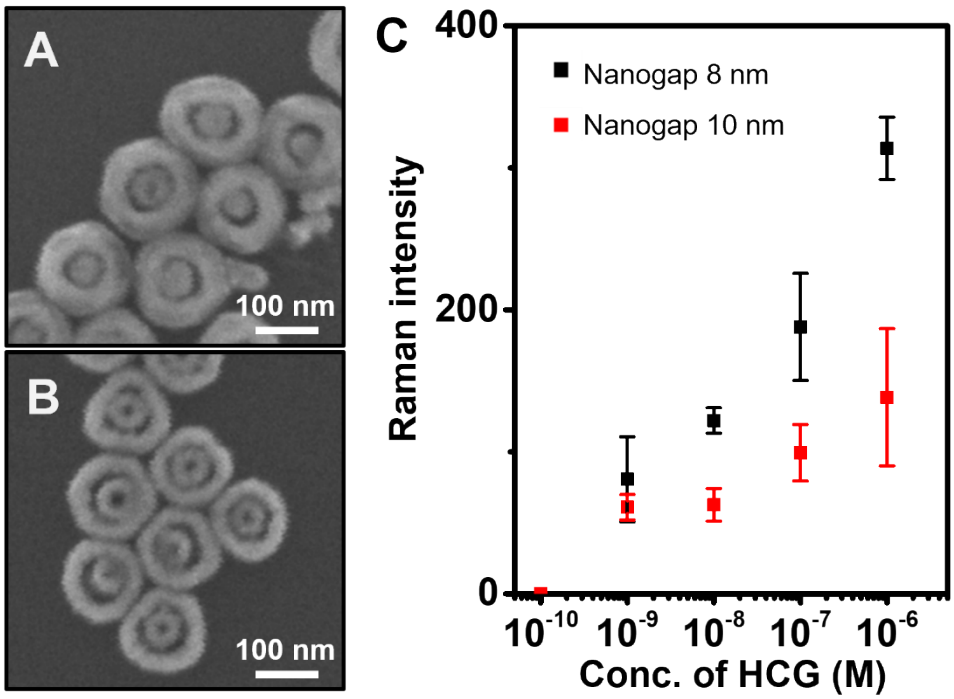

Figure S18. SERS-based immunoassay using Ag@Au hollow DRNs with intra-nanogaps of 8 nm and 10 nm. FE-SEM images of Ag@Au hollow DRNs with (A) 8 nm intra-nanogaps and (B) 10 nm intra-nanogaps. (C) Corresponding SERS-based immunoassay toward HCG (The intensity was plotted based on the peak at 1080 cm^{-1}). The sizes of nanogaps were estimated using image J program.

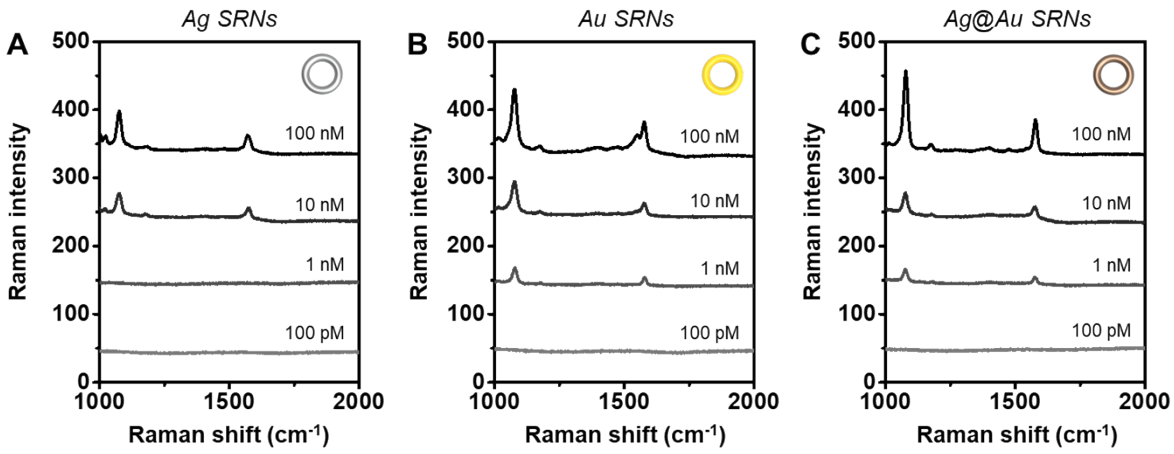

Figure S19. SERS-based immunoassay using SRNs. SERS spectra obtained from SERS-based immunoassay with (A) Ag SRNs, (B) Au SRNs, and (C) Ag@Au hollow SRNs.

References

1. S. Yoo, J. Kim, S. Choi, D. Park and S. Park,Two-dimensional nanoframes with dual rims, *Nat. Commun.,* 2019, **10**.
2. Q. F. Zhang, N. Large and H. Wang, Gold Nanoparticles with Tipped Surface Structures as Substrates for Single-Particle Surface-Enhanced Raman Spectroscopy: Concave Nanocubes, Nanotrisoctahedra, and Nanostars, *Acs. Appl. Mater. Inter.,* 2014, ***6*** (19), 17255-17267..
3. W. X. Niu, Y. A. A. Chua, W. Q. Zhang, H. J. Huang and X. M. Lu, Highly Symmetric Gold Nanostars: Crystallographic Control and Surface-Enhanced Raman Scattering Property, *J. Am. Chem. Soc.,* 2015, **137** (33), 10460-10463.
4. M. C. Schalnat and J. E. Pemberton, Comparison of a Fluorinated Aryl Thiol Self-Assembled Monolayer with Its Hydrogenated Counterpart on Polycrystalline Ag Substrates, *Langmuir* 2010, **26** (14), 11862-11869.